The Astrophysical Journal, 972:189 (12pp), 2024 September 10 https://doi.org/10.3847/1538-4357/ad6322

Competitive Entrapment of Hypervolatiles in Interstellar and Cometary Water Ice Analogs

Qijia Zhou, Alexia Simon, Karin I. Öberg, and Mahesh Rajappan
Center for Astrophysics | Harvard & Smithsonian, 60 Garden Street, Cambridge, MA 02138, USA; qijia.zhou@cfa.harvard.edu
Received 2023 December 14; revised 2024 July 3; accepted 2024 July 12; published 2024 September 9

Abstract

The distribution of chemical species in protoplanetary disks around young stars, especially their division between gas and solid phases, fundamentally shapes the composition of future planets and planetesimals. This distribution is likely affected by entrapment, a mechanism whereby volatile species are mechanically or chemically bound within a less volatile ice. In this study, we investigate the entrapment efficiencies of four hypervolatiles (CH_4, CO, N_2, and Ar) in multicomponent water ice mixtures deposited at different temperatures and mixture ratios. At low ice deposition temperatures, we observe small differences in entrapment efficiency (CH_4>CO>N_2∼Ar) up to a factor of two across species. The differences in entrapment between species increase by up to an order of magnitude with increasing deposition temperature. The relative entrapment efficiencies are also impacted by changes in the overall hypervolatile concentration of the ice mixtures. Collectively, these experiments suggest that relative entrapment efficiencies are mainly regulated by small differences in binding energies to the ice matrix, though competition for the best sites also influences entrapment in more concentrated ices. We use these results to better inform interpretations of hypervolatile observations in comets and related objects.

Unified Astronomy Thesaurus concepts: Astrochemistry (75); Planetary system formation (1257); Protoplanetary disks (1300); Planet formation (1241); Comet volatiles (2162); Chemical abundances (224); Laboratory astrophysics (2004)

1. Introduction

The disks of dust and gas that surround young stars are the birthplaces of planets. The distribution of chemical species between the solid and gas phase in these protoplanetary disks heavily influences planet and planetesimal formation (Lewis 1974; Dodson-Robinson et al. 2009). According to an ideal model with pure, unmixed elements in the system, the observed phase of an element can be predicted by an element's snowline (Lewis 1974; Sasselov & Lecar 2000; Öberg et al. 2011b). Hypervolatiles, or elements with extremely low sublimation temperatures, have snowlines that are very far away from the star (Öberg & Bergin 2021). In this scenario, we would generally not expect hypervolatiles to contribute to the formation of planetesimals and planet cores. However, observations of comets (Mousis et al. 2012; Lectez et al. 2015) and relatively high abundances of hypervolatiles in planets like Jupiter (Owen et al. 1999) cannot be explained by this simple model, suggesting that some mechanism must exist that brings solid-phase hypervolatiles inside their snowlines. One such mechanism is entrapment, where a hypervolatile is retained within another less volatile ice matrix and only sublimates during ice matrix reformation and/or at the snowline of the ice matrix (Bar-Nun et al. 1985).

Previous studies have used laboratory experiments to demonstrate that entrapment of hypervolatiles in water ice can be an efficient process (Bar-Nun et al. 1985, 1988, 2007; Ayotte et al. 2001; Collings et al. 2003, 2004; Fayolle et al. 2011; Fresneau et al. 2014; Almayrac et al. 2022; Simon et al. 2023; Gudipati et al. 2023). There is less consensus on the relative entrapment efficiencies of different hypervolatiles. Simon et al. (2023) found similar entrapment efficiencies in binary mixtures (i.e., one hypervolatile mixed in the ice matrix) of several astrophysically relevant hypervolatiles (CH_4, CO, N_2, and Ar) in water and CO_2 ices deposited at 10–30 K. This is in agreement with previous work on multicomponent ices (i.e., multiple hypervolatiles mixed in the ice matrix) at low temperatures by Bar-Nun et al. (1988), while more recent work by the same group (Bar-Nun et al. 2007) observed depletion of N_2 by a factor of 20–70 compared to CO. Studies investigating entrapment at higher ice deposition temperatures (Bar-Nun et al. 1988; Almayrac et al. 2022) also find large differences in entrapment.

When observed, differences in hypervolatile entrapment have been ascribed to differences in hypervolatile desorption temperature, binding energies, and mobility in the ice matrix (Bar-Nun et al. 2007; Almayrac et al. 2022). These can affect entrapment efficiencies in at least two distinct ways. In the first scenario, the absolute binding energy or desorption temperature of a hypervolatile determines its entrapment, and in this case the same entrapment efficiency should be observed in binary and multicomponent ices for a given hypervolatile. In the second scenario, the different hypervolatiles compete for strongly binding sites in the water ice, and so the relative binding energies of different hypervolatiles become important when predicting entrapment efficiencies. In this second case, we expect the entrapment efficiencies to depend on the precise mixture of hypervolatiles in water ice. The competitive effects should be especially pronounced in more concentrated ice mixtures, where a large number of hypervolatiles would be competing for a small number of strongly binding sites.

In this study, we explore differences in entrapment between hypervolatile species in three-component (two hypervolatiles mixed in water) and five-component (four hypervolatiles mixed

in water) ice mixtures. We aim to explore relative entrapment efficiencies of different hypervolatiles across a range of ice conditions and constrain the conditions under which competitive entrapment is significant. Our paper is organized as follows: in Section 2, we detail our experimental setup, design, and procedure, as well as our analysis methods. In Section 3, we present the results of our experiments, starting with three-component mixtures deposited at 12 K, followed by five-component mixtures deposited between 12 and 100 K, and finally five-component mixtures with different mixing ratios. In Section 4, we discuss possible physical–chemical origins of the observed results and the astrophysical implications.

2. Methods

2.1. Experimental Setup

This experimental setup is described in detail in Simon et al. (2023). Briefly, the experimental setup used for this project consists of a 6.″5 ultra-high vacuum (UHV) chamber, which can reach pressures as low as $\sim 4 \times 10^{-9}$ torr, mimicking the conditions of the interstellar medium and protoplanetary disks. A CsI substrate is suspended in a sample holder at the center of the chamber. The sample holder is attached to a cryostat and can be cooled to 12 K. The temperature of the sample holder and substrate is controlled between 12 and 300 K with ±0.1 K precision and ∼2 K absolute accuracy by a heater attached to the top of the sample holder. A gas doser is used to deposit the gas directly onto the substrate. The doser is a thin stainless steel tube positioned 2 inches from the substrate and perpendicular to its surface. The doser is connected to the gas line, which is a system of connected flasks, valves, and pressure gauges used to create gas mixtures with precise ratios. The base pressure of the gas line is $\sim 10^{-4}$ torr.

The two main instruments in our setup are the Fourier transform infrared (FTIR) spectrometer and the quadrupole mass spectrometer (QMS). The FTIR spectrometer monitors the ices and is used to derive the thickness of the IR-active ices, which allows us to calculate the mixing ratios. The QMS monitors the gases in the chamber, providing information about the gas composition during temperature-programmed desorption. The FTIR and QMS are separated by 90° within the chamber.

2.2. Experimental Procedure

The experiments in this study are temperature-programmed desorption (TPD) experiments, in which ice mixtures are deposited onto the sample holder and linearly heated until full desorption of the ice. We cool the substrate to the desired deposition temperature using the cryostat. Following Simon et al. (2023), we create the gas mixture by introducing specific amounts of the species of interest into the flasks and allowing the gases to mix inside the gas line. We deviate slightly from this procedure for the five-component mixtures, since there are only three flasks attached to the gas line. In the five-component experiments, we collect CH_4, N_2, and Ar in the flasks, while we introduce CO and water directly to the gas line before mixing. Gases are allowed to mix for about an hour before deposition. The experiments were performed using $^{12}CH_4$ (99.9% purity, Sigma-Aldrich), ^{13}CO (99% purity, Sigma-Aldrich), $^{15}N_2$ (98% purity, Sigma-Aldrich), Ar (99.95% purity, Sigma-Aldrich), and deionized H_2O. In this experiment, ^{13}CO ($m/z = 29$) is used instead of ^{12}CO ($m/z = 28$) and $^{15}N_2$ ($m/z = 30$) is used instead of $^{14}N_2$ ($m/z = 28$), to prevent atmospheric nitrogen from interfering with our observations. The gas is deposited onto the substrate at a median rate of ∼40 ML min^{-1}, or ∼0.02 μm min^{-1}. During ice deposition, we use the FTIR spectrometer to rapidly take IR spectra in order to monitor the approximate thickness of the ice (see Section 2.3 for the procedure to determine ice thickness).

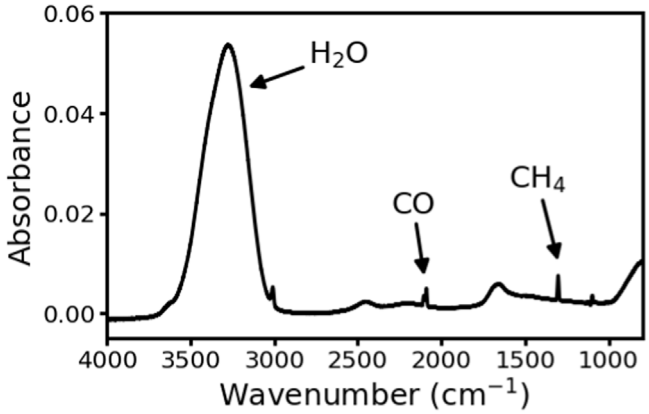

Figure 1. The after-dose IR spectra of H_2O:CH_4:^{13}CO from 800 cm^{-1} to 4000 cm^{-1}. The CH_4, CO, and H_2O features used to determine the ice matrix thickness and the ice mixture composition are marked.

Following deposition, we turn the sample holder so that the IR ray is perpendicular to the ice surface, in order to obtain a precise measurement of the final ice thickness without the complications induced by refraction through the ice sample. We turn the sample holder to 45° with respect to the IR for the TPD phase of our experiment, so we can observe the ice desorption process with both the QMS and IR spectrometers. During the TPD phase, we linearly heat the sample holder at a rate of 1 K min^{-1} until the sample holder reaches 200 K and all components have desorbed.

2.3. Determination of Ice Column Density

The thickness of the ice and the ice mixing ratio of the IR-active species (H_2O, CH_4, and CO) can be determined from the IR spectra. IR observations of each experiment are taken at 0.5 cm^{-1} resolution from 800 cm^{-1} to 4000 cm^{-1}. One example is Figure 1, which displays the IR spectra of the H_2O:CH_4:CO mixture immediately after deposition at 12 K and notes the features corresponding to each species. To remove background FTIR signal, we subtract the mean absorbance of the continuum near each feature.

To determine the thickness of the ice, we use Equation (1), which relates the ice thickness for a specific species i to the integrated absorbance under the corresponding IR peak:

$$N(i) = \frac{2.3}{A(i)} \int \mathrm{Abs}(\tilde{\nu}) d\tilde{\nu}, \quad (1)$$

where $N(i)$ is the column density in molecules cm^{-2}, $\int \mathrm{Abs}(\tilde{\nu}) d\tilde{\nu}$ is the integrated area under the IR absorbance peak in cm^{-1}, and $A(i)$ is the band strength of the species in cm molecule^{-1}. All of the immediate post-deposition IR spectra were obtained with the IR field vector perpendicular to the sample holder surface. The band strengths of H_2O, CH_4, and ^{13}CO are listed in Table 1. The column density can be converted to an ice thickness in monolayers (ML) assuming a standard 10^{15} molecules cm^{-2} per ML. The water and

Table 1
Band Positions and Strengths of Relevant IR-active Species

Species	Band pos. (cm^{-1})	Strength (cm $molecule^{-1}$)
H_2O	3000–3600	2.2×10^{-16}
CH_4	1290–1320	8.4×10^{-18}
^{13}CO	2080–2110	1.4×10^{-17}

Note. Band strengths from Hudgins et al. (1993) and Gerakines et al. (1995), corrected for ice density in Bouilloud et al. (2015).

hypervolatile column density ratios give the initial deposited mixing ratios if the ice is deposited at or below 30 K, i.e., at a low enough temperature that there is no substantial hypervolatile desorption during ice deposition.

For the two IR-inactive hypervolatiles, Ar and N_2, we instead use the QMS to determine the ice mixing ratio. This requires the QMS signal to be calibrated, and we use the CO-based calibration method as introduced by Martín-Doménech et al. (2015) and explained in detail for our setup in Simon et al. (2023). The relationship between N(mol), the thickness of the ice in ML, and $A(m/z)$, the integrated area underneath the TPD QMS curve for a specific m/z, is described in the following equation:

$$N(\text{mol}) = A(m/z) \times \frac{1}{k_{\text{CO}}} \times \frac{\sigma^{+}(\text{CO})}{\sigma^{+}(\text{mol})} \times \frac{I_F(\text{CO}^{+})}{I_F(\text{mol})} \times \frac{F_F(\text{CO})}{F_F(\text{mol})} \times \frac{S(29)}{S(m/z)}, \quad (2)$$

where k_{CO} is an experiment-specific proportionality factor, σ^{+}(mol) is ionization cross section for the first ionization of the species at the incident electron energy of the mass spectrometer (70 eV for our setup), I_F(mol) is the fraction of ionized molecules with charge z, F_F(mol) is the fraction of molecules leading to a fragment of mass m in the QMS, and $S(m/z)$ is the sensitivity of the QMS instrument to a mass fragment m/z. Here, $A(m/z)$ is determined from integrating the entire TPD QMS curve. The values of σ^{+}(mol), I_F(mol), F_F(mol), and $S(m/z)$ for the relevant species are stated in Simon et al. (2023). The proportionality constant k_{CO} can be calculated using N(CO), which is derived from the IR spectra using Equation (1), and $A(m/z = 29)$:

$$k_{\text{CO}} = \frac{A(m/z = 29)}{N(\text{CO})}. \quad (3)$$

For three-component mixtures without CO, the QMS signals are calibrated with the average k_{CO} from the three-component experiments with CO. For ices deposited above 30 K, the QMS signals are calibrated with the average k_{CO} from the five-component experiments at 12 K. Since some hypervolatiles desorb during ice deposition at higher temperatures, the hypervolatile column densities derived from the after-dose IR spectra and the integrated TPD curves are no longer representative of the deposited hypervolatile column densities. We estimate the initial hypervolatile column densities by assuming we obtained the desired gas mixing ratio and multiplying this ratio by the water ice thickness.

2.4. Entrapment Efficiency and Error Calculation

The entrapment efficiencies of the hypervolatiles can be calculated from the TPD QMS data (Simon et al. 2019, 2023). The QMS counts per time unit are proportional to the rate of hypervolatile desorption. Since we increase the temperature of the sample holder at a constant rate, the integrated area under the TPD curve between two temperatures is proportional to the number of molecules desorbed in that temperature range. To remove any background QMS signal, we fit a linear baseline and subtract it from the TPD curve. The baseline is fitted to the values in the temperature ranges 15–20 K and 180–190 K for the low-temperature experiments and the ranges 130–140 K and 180–190 K for the high-temperature experiments.

We define entrapment efficiency as the ratio between the number of hypervolatile molecules entrapped in the ice matrix and the total number of hypervolatile molecules initially deposited. For ices deposited at or below 30 K, the full integrated TPD curve is proportional to the total number of hypervolatile molecules deposited onto the substrate. For each hypervolatile, the first peak around the desorption temperature of the hypervolatile coincides with the free molecules desorbing from the surface of the ice. The second peak around the desorption temperature of water (~160 K) coincides with the desorption of the entrapped hypervolatiles,[1] and so the integrated area of the second peak is proportional to the number of entrapped molecules. For ices deposited above 30 K, the full integrated TPD curve no longer represents the total deposited hypervolatiles, and we instead calculate the entrapment efficiency as the ratio between the number of molecules in the entrapped desorption peak over the estimated total number deposited. This introduces a larger uncertainty in the entrapment efficiencies of these "warm" experiments compared to the cold-deposited ones.

More generally, we estimate that the most important sources of error are differences in gas mixture ratios used for different experiments and small day-to-day variations in the experimental setup, which especially affects the QMS calibration. We expect both of these to vary randomly and therefore estimate the error in entrapment efficiencies through repeat experiments spread out through the experimental series. The resulting dispersion calculations for each set of experiments are reported in Section 3.

3. Results

The goal of this series of experiments is to systematically examine hypervolatile entrapment in multicomponent mixtures and evaluate whether competitive entrapment between different hypervolatiles is important when estimating entrapment efficiencies. We do this in four stages: (1) three-component ice mixtures deposited at 12 K, (2) five-component mixtures deposited at 12 K, (3) five-component mixtures deposited at varying temperatures, and (4) five-component mixtures with varying mixture ratios.

[1] In all of our experiments, the desorption of the entrapped hypervolatiles slightly precedes the onset of water desorption. This is because most of the entrapped molecules are outgassed during water crystallization, and only a small amount co-desorbs with water (see Figure A1).

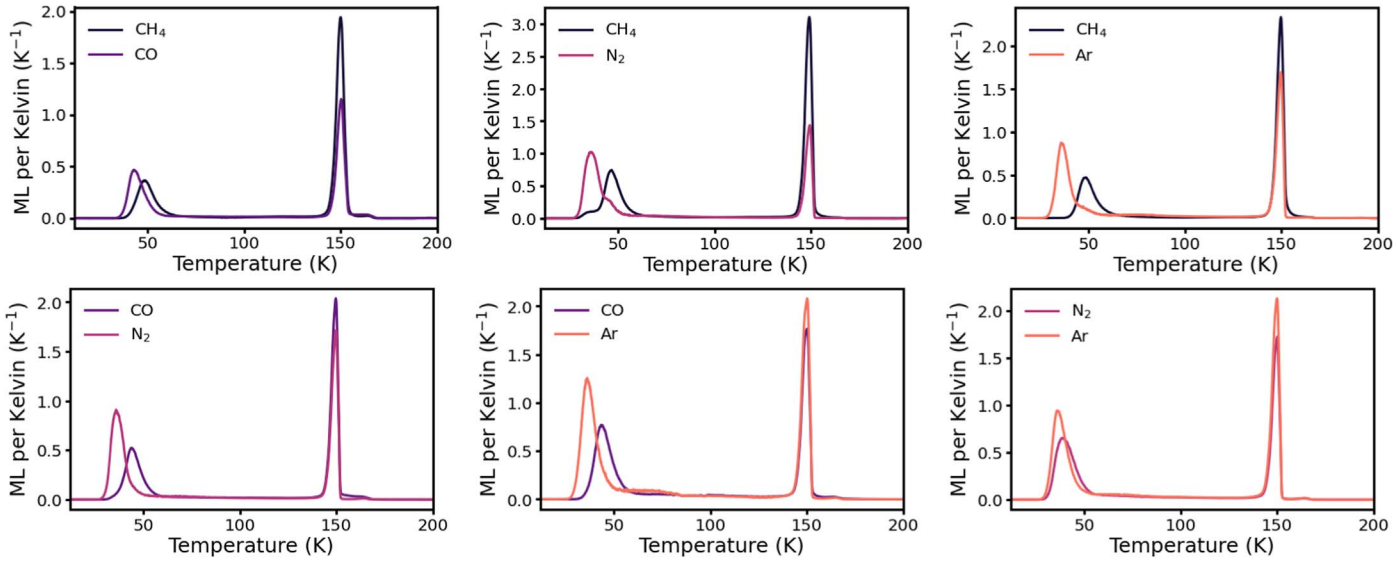

Figure 2. TPD curves for the three-component ice mixtures deposited at 12 K and at a ratio of 10:1:1. The TPD curves for H_2O are omitted from these plots to highlight the features of the hypervolatile TPD curves. See Figure A1 for TPD curves of repeated experiments with the H_2O curves included.

Table 2
Calculated Entrapment Efficiencies for the Full Series of Experiments

Mixture	Ratio	Dep. Temp	H_2O (ML)	CH_4 Entrap.	CO Entrap.	N_2 Entrap.	Ar Entrap.
H_2O:CH_4:^{13}CO	10:0.9:0.7	12 K	172	66% ± 3%	51% ± 3%	⋯	⋯
H_2O:CH_4:$^{15}N_2$	10:1.4:1.1	12 K	168	59% ± 3%	⋯	32% ± 2%	⋯
H_2O:CH_4:Ar	10:1.1:1.1	12 K	144	63% ± 3%	⋯	⋯	42% ± 2%
H_2O:^{13}CO:$^{15}N_2$†	10:1.0:1.0	12 K	165	⋯	56% ± 3%	43% ± 2%	⋯
H_2O:^{13}CO:$^{15}N_2$	10:1.1:1.1	12 K	160	⋯	54% ± 3%	39% ± 2%	⋯
H_2O:^{13}CO:$^{15}N_2$	10:1.0:1.0	12 K	289	⋯	57% ± 3%	45% ± 2%	⋯
H_2O:^{13}CO:Ar†	10:1.1:1.4	12 K	188	⋯	44% ± 2%	⋯	39% ± 2%
H_2O:^{13}CO:Ar	10:1.1:1.4	12 K	226	⋯	45% ± 2%	⋯	40% ± 2%
H_2O:$^{15}N_2$:Ar	10:1.1:1.3	12 K	170	⋯	⋯	43% ± 2%	45% ± 2%
H_2O:CH_4:^{13}CO:$^{15}N_2$:Ar	20:0.5:0.5:0.5:0.6	12 K	159	75% ± 11%	63% ± 9%	56% ± 8%	60% ± 9%
H_2O:CH_4:^{13}CO:$^{15}N_2$:Ar	20:1.0:1.1:1.1:1.2	12 K	143	69% ± 10%	47% ± 7%	39% ± 6%	45% ± 7%
H_2O:CH_4:^{13}CO:$^{15}N_2$:Ar†	20:1.0:0.9:1.1:1.2	12 K	118	67% ± 10%	49% ± 7%	40% ± 6%	46% ± 7%
H_2O:CH_4:^{13}CO:$^{15}N_2$:Ar	20:0.6:0.9:0.6:0.7	30 K	390	74% ± 11%	51% ± 8%	57% ± 9%	63% ± 9%
H_2O:CH_4:^{13}CO:$^{15}N_2$:Ar†	20:1.1:1.0:1.2:1.3	30 K	164	71% ± 11%	38% ± 6%	33% ± 5%	41% ± 6%
H_2O:CH_4:^{13}CO:$^{15}N_2$:Ar	20:1:1:1:1*	40 K	189	84% ± 28%	41% ± 14%	8.9% ± 3.0%	22% ± 7%
H_2O:CH_4:^{13}CO:$^{15}N_2$:Ar†	20:1:1:1:1*	40 K	129	75% ± 25%	26% ± 9%	2.3% ± 0.8%	7.8% ± 2.6%
H_2O:CH_4:^{13}CO:$^{15}N_2$:Ar	20:1:1:1:1*	50 K	137	35% ± 12%	14% ± 5%	0.6% ± 0.2%	1.3% ± 0.5%
H_2O:CH_4:^{13}CO:$^{15}N_2$:Ar†	20:1:1:1:1*	50 K	174	62% ± 21%	12% ± 4%	1.0% ± 0.3%	2.8% ± 1.0%
H_2O:CH_4:^{13}CO:$^{15}N_2$:Ar	20:1:1:1:1*	50 K	179	60% ± 20%	4.6% ± 1.6%	0.8% ± 0.3%	2.2% ± 0.7%
H_2O:CH_4:^{13}CO:$^{15}N_2$:Ar	20:1:1:1:1*	60 K	260	14% ± 5%	1.4% ± 0.5%	0.2% ± 0.1%	0.3% ± 0.1%
H_2O:CH_4:^{13}CO:$^{15}N_2$:Ar	20:1:1:1:1*	80 K	147	< 0.2%	< 0.2%	< 0.2%	< 0.2%
H_2O:CH_4:^{13}CO:$^{15}N_2$:Ar	20:1:1:1:1*	100 K	224	< 0.2%	< 0.2%	< 0.2%	< 0.2%
H_2O:CH_4:^{13}CO:$^{15}N_2$:Ar	20:0.3:0.3:0.3:0.3*	50 K	302	70% ± 24%	24% ± 8%	4.3% ± 1.5%	8.6% ± 2.9%
H_2O:CH_4:^{13}CO:$^{15}N_2$:Ar	20:3:3:3:3*	50 K	129	13% ± 4%	2.6% ± 0.9%	0.1% ± 0.04%	0.3% ± 0.1%

Notes. Ice mixing ratios are calculated by finding the ratios between the hypervolatile ice thicknesses and the water ice thickness. The ice thicknesses are measured in monolayers (ML), where one monolayer is equivalent to a column density of 10^{15} molecules cm^{-2}. When there are repeated experiments, the dagger (†) indicates the experiment for which the TPD curve is plotted in the main text. The other TPD curves are in the Appendix. A star (*) next to the ratio indicates that the true ratio is unknown, but we assume that the real mixture ratio is the same as the aim ratio. Error calculation is described in Section 2.4 and throughout Section 3.

3.1. Entrapment Efficiencies in Three-component Ice Mixtures Deposited at 12 K

We determine the entrapment efficiencies in six distinct three-component mixtures with a water:hypervolatile:hypervolatile ratio of 10:1:1 deposited at 12 K: H_2O:CH_4:CO, H_2O:CH_4:N_2, H_2O:CH_4:Ar, H_2O:CO:N_2, H_2O:CO:Ar, and H_2O:N_2:Ar. The H_2O:CO:N_2 experiment was conducted three times, the H_2O:CO:Ar experiment twice, and the rest once. For each experiment, we use the IR spectra and integrated QMS curves to derive the ice thicknesses and precise mixing ratio (Section 2.3). To estimate the error in our entrapment efficiencies, we calculate

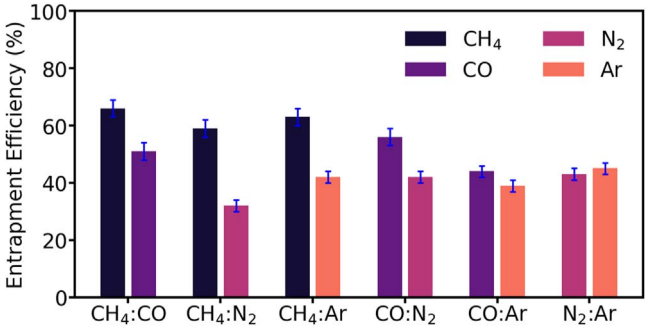

Figure 3. Comparison of entrapment efficiencies in three-component experiments at 12 K and at a ratio of 10:1:1.

the fractional dispersion of the entrapment efficiencies for CO and N_2 in the H_2O:CO:N_2 experiment. The average fractional dispersion for CO and N_2 is 5%.[2] Since we do not expect the dispersion to depend on species, we propagate the average error for CO and N_2 to all hypervolatiles in the other experiments.

The TPD profiles for the full suite of three-component experiments are plotted in Figure 2, and the calculated entrapment efficiencies are recorded in Table 2. Figure 3 compares the average entrapment efficiencies in the three-component experiments. The resulting entrapment efficiency across different experiments is 59%–66% for CH_4, 44%–57% for CO, 39%–45% for Ar, and 32%–45% for N_2. Across the three-component experiments, there are small but consistent differences in entrapment between hypervolatiles, with CH_4 better entrapped than CO, N_2, and Ar by up to a factor of two, and CO better entrapped than N_2 and Ar. However, there is no obvious pattern in the entrapment efficiencies dependent on which hypervolatiles are in the ice mixture, which would be expected if competitive entrapment is important, i.e., Ar and N_2 entrapment is generally similar whether mixed with a more strongly entrapped hypervolatile (CH_4 or CO) or with each other. The one possible exception is N_2 mixed with CH_4, which does appear substantially less entrapped in this mixture compared to the two other ones. The significance of this difference is difficult to ascertain from a single experiment, however, and we return to this question in Section 4.1 where we discuss what evidence exists for competitive entrapment across the experimental series.

3.2. Entrapment Efficiencies in Five-component Ice Mixtures Deposited at 12 K

We conducted three experiments with the five-component ice mixture, H_2O:CH_4:CO:N_2:Ar, deposited at 12 K at a ratio of 20:1:1:1:1. The TPD curves for one of the five-component experiments at 12 K is plotted in the top panel of Figure 4, and the full suite of experiments is plotted in Figure A2. To estimate the error, we calculate the entrapment dispersions from the three experiments for each hypervolatile. We then assume that the error is the same for all hypervolatiles and average the dispersions to calculate a single error of 15%, which we apply to the entrapment efficiencies of the three experiments in Table 2. We think this larger dispersion compared to the three-component experiments is due to a larger variation in mixture composition in this more complex set of experiments. The

[2] To find the dispersion for a specific entrapment efficiency, we multiply the efficiency by the fractional dispersion. Thus, for an entrapment efficiency of 50% and a fractional dispersion of 5%, the dispersion is 2.5%.

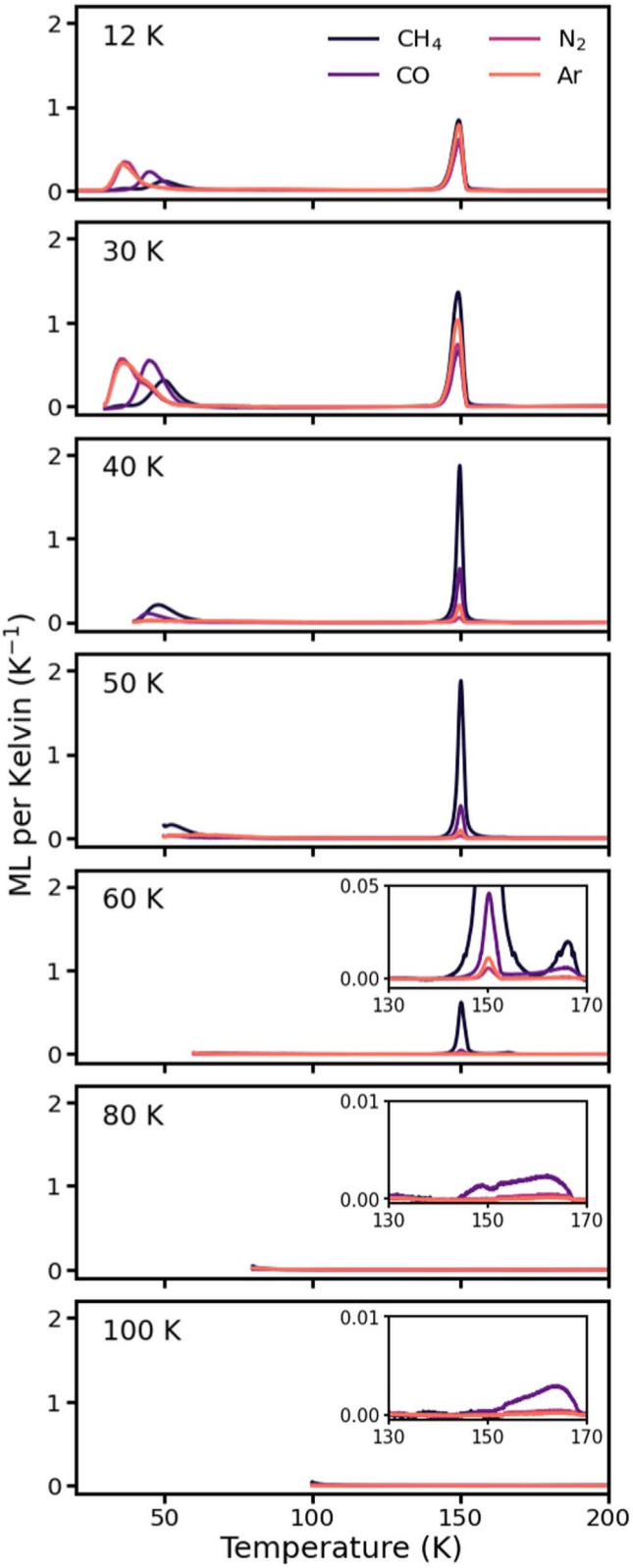

Figure 4. TPD curves for CH_4, CO, N_2, and Ar in the five-component ice mixtures deposited at 12 K, 30 K, 40 K, 50 K, 60 K, 80 K, and 100 K, at a ratio of 20:1:1:1:1. See Figure A2 for TPD curves of repeated experiments.

average entrapment efficiencies in the five-component experiments at 12 K are shown in Figure 5.

Similar to the three-component mixtures, CH_4 is the best-entrapped (70%), then CO (53%), followed by Ar and N_2 (50%

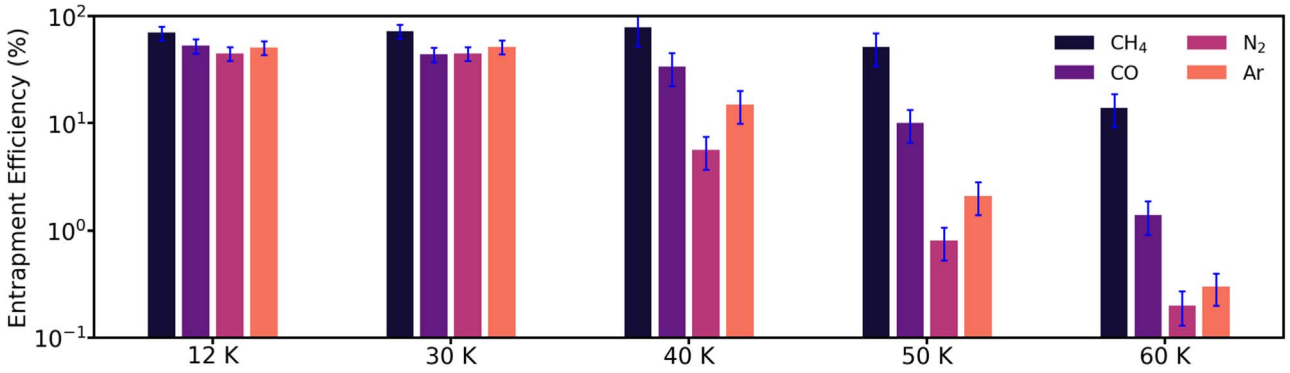

Figure 5. Comparison of entrapment efficiencies in five-component experiments at various deposition temperatures and at a ratio of 20:1:1:1:1.

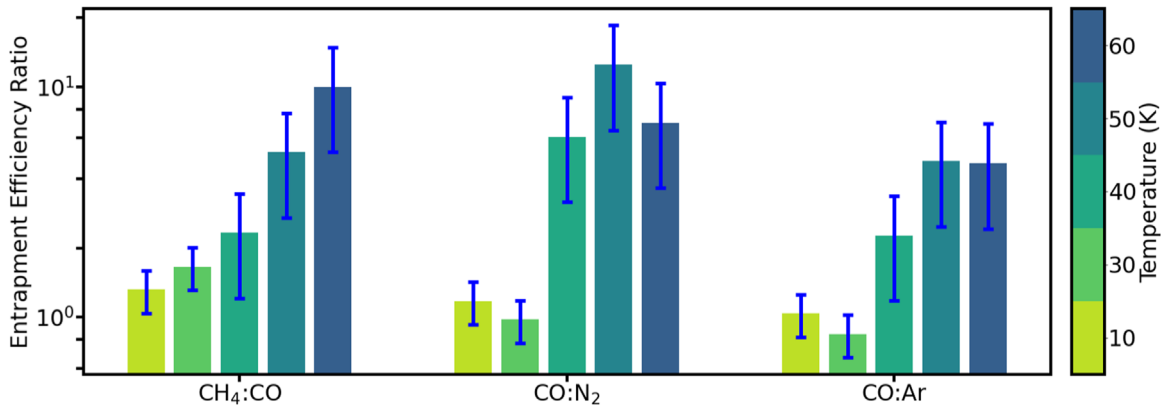

Figure 6. Comparison of the entrapment efficiency ratios for astrophysically relevant pairs of hypervolatiles at different deposition temperatures. The ratios are calculated in the order that they are represented along the horizontal axis.

and 45%, respectively). The entrapment differences between CH_4 and the other three hypervolatiles are significant, though not as dramatic as in the three-component experiments, while the CO, N_2, and Ar entrapment efficiencies are statistically indistinguishable under these ice conditions. However, we note that, in all experiments, CO is better entrapped than N_2 and Ar.

3.3. Entrapment Efficiencies in Five-component Ice Mixtures Deposited at Higher Temperatures

In the third series of experiments, we use the five-component ice mixture H_2O:CH_4:CO:N_2:Ar at a ratio of 20:1:1:1:1, and we vary the deposition temperature, i.e., the temperature of the substrate during ice deposition. We tested deposition temperatures ranging from 12 K to 100 K. The TPD profiles at each temperature are shown in Figure 4. We conducted the 50 K experiment three times and used the average fractional dispersion of 34% to estimate entrapment uncertainties for all hypervolatiles in experiments deposited between 40 and 100 K. The entrapment efficiencies and their estimated uncertainties are recorded in Table 2. For experiments where we do not observe a clear entrapment peak (80–100 K), we estimate an upper limit to the entrapment. This estimation is complicated by correlated noise distorting the baseline (see insets in Figure 4), and therefore we take a conservative approach and set our upper limits to the minimum level of entrapment observed at 60 K, i.e., 0.2%. Figure 5 compares the average entrapment efficiencies in the five-component experiments at various deposition temperatures. At all temperatures where some entrapment is observed, CH_4 is entrapped most efficiently followed by CO, Ar, and N_2, which is the same trend observed at lower temperatures. However, relative entrapment efficiencies between species change with ice formation temperature. In Figure 5, we observe that CH_4 entrapment is constant up until 50 K, and still substantial at 60 K. CO entrapment begins decreasing at 50 K, and Ar and N_2 entrapment is low already at 40 K. This leads to an increasing entrapment difference between different hypervolatiles with increasing temperature between 30 and 60 K. At 12 K, CH_4 is only entrapped 10%–20% better than the other hypervolatiles, while at 50 K, it is entrapped more than an order of magnitude better than Ar and N_2. Figure 6 compares the entrapment efficiency ratios of astrophysically relevant pairs of hypervolatile species at different deposition temperatures.

We note that, while the primary peak of hypervolatile desorption precedes the onset of water desorption, as entrapped hypervolatiles are released during crystallization, there is a noticeable second release of CH_4 and CO for the experiments at 60 K, 80 K, and 100 K. This second peak coincides with the water desorption peak at ~160 K and results from a small amount of entrapped hypervolatiles co-desorbing with the ice. See Figure A1 for further discussion.

3.4. Entrapment Efficiencies in Five-component Ice Mixtures with Varying Mixture Ratios

In the fourth series of experiments, we use the five-component ice mixture H_2O:CH_4:CO:N_2:Ar, depositing the ice at 50 K with different ice mixture ratios of 20:0.3:0.3:0.3:0.3 (dilute), 20:1:1:1:1 (standard), and 20:3:3:3:3 (concentrated), to explore the

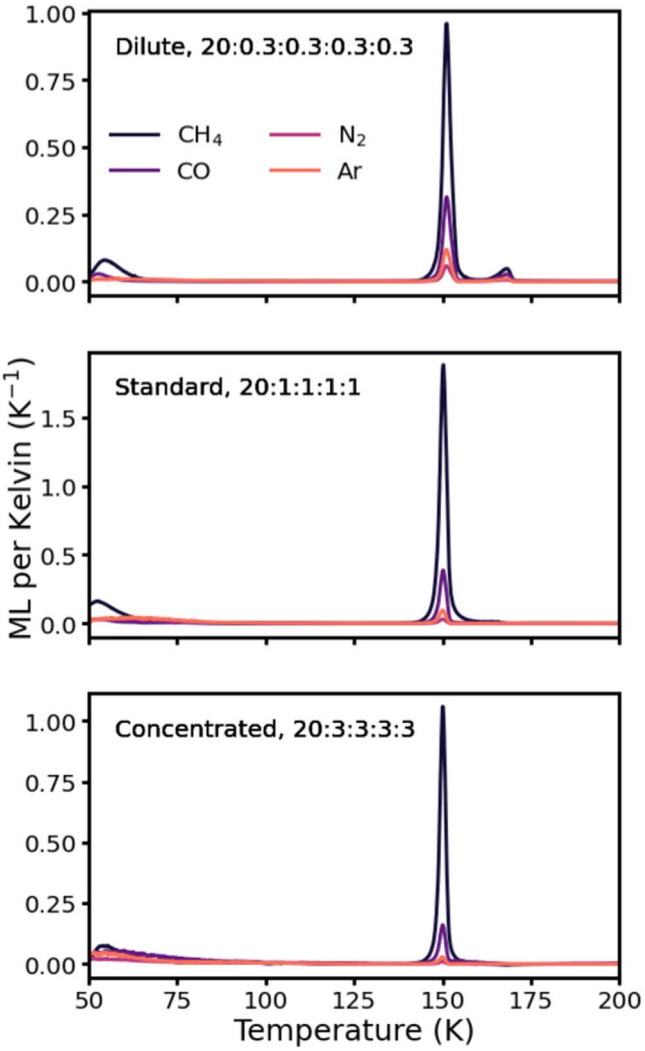

Figure 7. TPD curves for the five-component ice mixtures deposited at 50 K and at various ratios: dilute (20:0.3:0.3:0.3:0.3), standard (20:1:1:1:1), and concentrated (20:3:3:3:3).

effect of hypervolatile concentration on entrapment. The TPD profiles at each ratio are shown in Figure 7. Figure 8 compares the entrapment efficiencies at varying mixture ratios. We use the fractional dispersion derived from the five-component 20:1:1:1:1 experiments at 50 K to calculate the entrapment uncertainty for all experiments and hypervolatiles. All calculated entrapment efficiencies are recorded in Table 2.

The ordering of entrapment efficiencies between species is consistent across the varying mixture ratios, with the most to the least entrapped being CH_4, CO, Ar, and N_2. However, increasing the concentration of hypervolatiles decreases the overall entrapment efficiency across all species. There is also some difference in the relative entrapment between the three experiments. We plot the ratios between the entrapment efficiencies for astrophysically relevant hypervolatile pairs and compare them across the dilute, standard, and concentrated experiments in Figure 9. The errors for each ratio are derived from propagating the errors from the individual entrapment efficiencies.

From Figure 9, there appears to be some correlation between the entrapment efficiency ratio and the mixture ratio, such that the entrapment differences become more pronounced for more

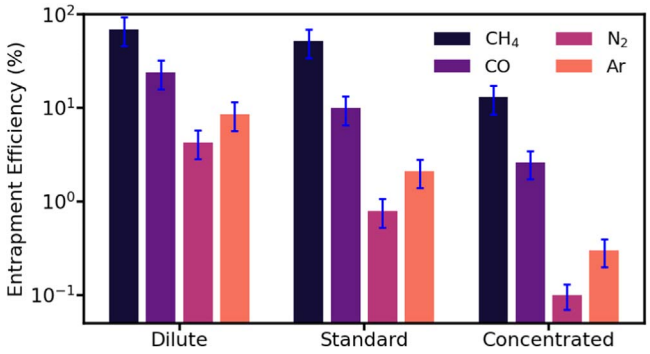

Figure 8. Comparison of entrapment efficiencies in five-component experiments deposited at 50 K and at various ratios: dilute, standard, and concentrated.

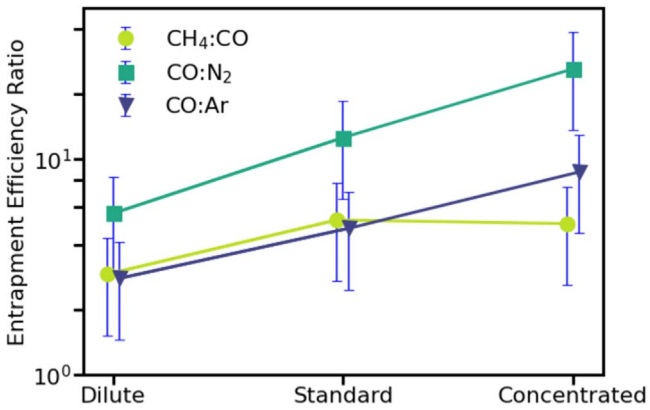

Figure 9. The entrapment efficiency ratios for astrophysically relevant pairs of hypervolatiles, compared across the dilute, standard, and concentrated experiments.

concentrated mixtures. This is especially true when comparing CO and N_2 entrapment. These results suggest that increasing the hypervolatile concentration of the ice mixture increases the relative entrapment efficiency ratio between species, and that competitive entrapment thus plays a role in concentrated ice mixtures.

4. Discussion

We discuss the observed entrapment behaviors and potential explanations for entrapment differences in cold ices deposited between 10 and 30 K in Section 4.1 and warm ices deposited above 30 K in Section 4.2. We then present astrophysical implications and applications of our findings in Section 4.3.

4.1. Entrapment in Ices Deposited between 12 and 30 K

For three- and five-component ices deposited at 12–30 K, we find that CH_4 is consistently better entrapped than CO, and CO is better entrapped than Ar and N_2. The largest difference is seen for CH_4 and N_2 in the corresponding three-component mixture and one of the five-component mixtures deposited at 30 K, where CH_4 is better entrapped by a factor of two. In the remaining experiments, the differences are around 20%–50%.

We consider two possible explanations for the observed differences in entrapment efficiency across species, both of which are related to the hypervolatile binding energies. Our focus on binding energies is based on the observation that the

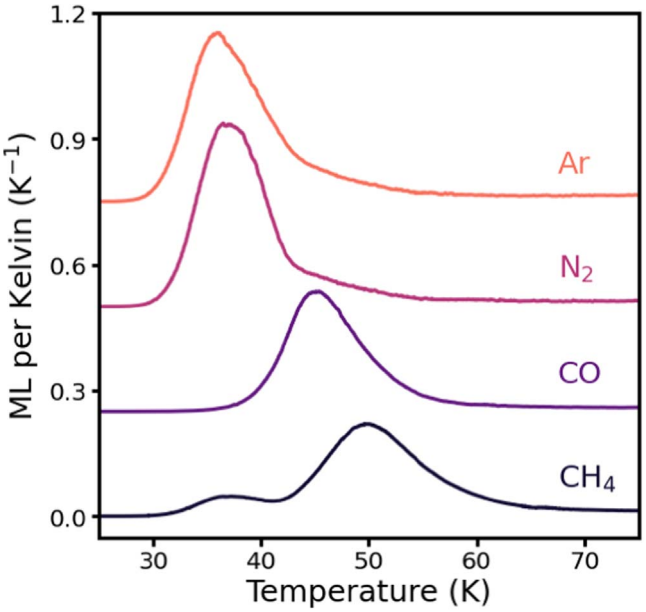

Figure 10. The initial desorption peaks from one of the five-component experiments deposited at 12 K, with a uniform offset for each TPD curve.

order of increasing entrapment efficiency is identical to the order of increasing desorption temperature of the first hypervolatile peak (Ar $\leqslant$ N_2 < CO < CH_4). The peak of the hypervolatile desorption feature can be used as a rough proxy for binding energy between the hypervolatile and the ice matrix (Collings et al. 2004; Villadsen et al. 2022). The initial desorption peaks from one of the five-component experiments at 12 K are plotted in Figure 10.

Intuitively, stronger bonding should lead to more entrapment regardless of whether there are competitors. For example, this effect is seen when comparing CO and CO_2 entrapment in H_2O ice (Fayolle et al. 2011). Small differences in the weak interactions between hypervolatile and water molecules may therefore drive differences in entrapment efficiencies (Rowland et al. 1991; Bar-Nun & Owen 1998). In this case, the differences in the entrapment efficiencies across species should be independent of the ice composition as long as the overall hypervolatile-to-water ratio is the same. Another possible explanation for differences in entrapment efficiencies is the presence of competitive entrapment, where hypervolatiles compete for the best binding sites (Lunine & Gautier 2004; Bar-Nun et al. 2007). In this scenario, the entrapment efficiency of a given hypervolatile should decrease in the presence of a more strongly binding molecule—and vice versa—when all other parameters, including the total hypervolatile concentration, are held constant.

If competitive entrapment is insignificant, we should observe the same entrapment efficiencies in binary and multicomponent ice mixtures. Superficially, this is contradicted by comparing our 12 K three-component mixture results with those of Simon et al. (2023), who claimed to find no significant differences in entrapment efficiency between hypervolatiles in binary mixtures. The discrepancy between these results, however, may be explained by the sensitivity of the entrapment efficiency to experimental parameters such as ice thickness and composition. In the binary mixture experiments most similar to ours (10:1 mixtures deposited at 10 K), CH_4, CO, and N_2 entrapment efficiencies are ∼60% and Ar ∼40%, so all but the entrapment of N_2 agree with our results within uncertainties (Simon et al. 2023). We speculate that the relatively high N_2 entrapment efficiency in Simon et al. (2023) is due to a somewhat thicker and more dilute ice mixture in their H_2O:N_2 experiment compared to the other CH_4, CO, and Ar experiments. Another argument against competitive entrapment is the fact that we do not see changing entrapment efficiencies between the different three-component mixtures, with the possible exception of N_2 mixed with CH_4. Thus, we cannot conclude that there is a significant dependence on ice composition for entrapment efficiencies at low temperatures, and hence that there is clear evidence for competition under these ice conditions.

We note that there are two earlier sets of experiments on multicomponent ice mixtures, and in both cases their results are in tension with ours. Bar-Nun et al. (1988) found no differences in entrapment efficiencies in a mixture of CH_4, CO, N_2, and Ar deposited between 24 and 35 K, while Bar-Nun et al. (2007) found an order-of-magnitude depression in N_2 entrapment in a mixture of CO, N_2, and Ar deposited at 30 K. Our findings appear to fall between the two extremes: we do observe small differences in entrapment efficiency across species in multicomponent mixtures, unlike Bar-Nun et al. (1988), yet we do not observe the large difference in entrapment efficiency reported in Bar-Nun et al. (2007). Our calculated entrapment efficiency of CO is higher than that of N_2 in every experiment, but the maximum difference is on the order of twofold rather than the 20–70× difference observed by Bar-Nun et al. (2007) 's observed. We note that both Bar-Nun et al. (1988) and Bar-Nun et al. (2007) used much more concentrated ice mixtures, such that the total hypervolatile load was greater than or equal to the amount of matrix material. Based on the results of our experiments at various mixture ratios, we theorize that entrapment efficiencies may be very sensitive to the precise experimental conditions at very high hypervolatile concentrations, which might explain the large disagreement between the results of Bar-Nun et al. (1988) and Bar-Nun et al. (2007). To test this would require additional experiments, but we note that, in most astrophysical environments, hypervolatiles should be present in dilute concentrations based on interstellar measurements of CO and CH_4 mixing ratios with water (Pontoppidan et al. 2005; Öberg et al. 2011a).

An additional reason for differences between these entrapment experiments may be different deposition rates. Our deposition rate of $\sim 0.02\ \mu m\ min^{-1}$ falls in between the deposition rate of Bar-Nun et al. (1988) ($\sim 0.11\ \mu m\ min^{-1}$) and the deposition rate of Bar-Nun et al. (2007) ($\sim 5 \times 10^{-4}\ \mu m\ min^{-1}$). Hypervolatile entrapment can be sensitive to deposition rate; when depositing at temperatures below 27 K, Notesco et al. (2003) find that the entrapment of Ar in water is lower at a deposition rate of $\sim 10^{-5}\ \mu m\ min^{-1}$ compared to that at higher deposition rates. The authors suggest that, at very low deposition rates, background N_2 and CO can successfully compete with Ar for entrapment sites. In addition, Gerakines & Hudson (2015) find that depositing CH_4 at a rate exceeding $0.12\ \mu m\ min^{-1}$ can create crystalline (rather than amorphous) ice, even at temperatures below 20 K. Gerakines et al. (2023) observe a similar sensitivity to deposition rate when forming amorphous CO ice. Thus, variations in deposition rate can change the phase (crystalline versus amorphous) of the deposited ices, which can influence its entrapment behavior. In conclusion, there are small (up to a factor of two) but real differences in hypervolatile entrapment

in dilute, multicomponent ice mixtures deposited at low temperatures. At our experimental conditions, we find no evidence that these differences are enhanced due to competitive entrapment, and instead we ascribe them to small differences between hypervolatile binding energies.

4.2. Entrapment in Ices Deposited Above 30 K

For five-component ice mixtures deposited above 30 K, CH_4 is entrapped most efficiently followed by CO, Ar, and N_2 at all temperatures where some entrapment is observed. We also observe increasing entrapment differences between hypervolatiles species at higher deposition temperatures. Similar to the low-temperature ices, we propose that this pattern can be explained in terms of hypervolatile binding energies to the water ice matrix, but suggest that the most important effect is the difference in desorption rate during deposition. During deposition above 30 K, the hypervolatile desorption rate is proportional to $e^{-E_{\rm des}/T}$, where $E_{\rm des}$ is the binding energy and T is the temperature. This implies that the residence time, which is inversely proportional to desorption rate, decreases exponentially with decreasing binding energy. Species with lower desorption temperatures (i.e., N_2 and Ar) have shorter residence times and are therefore much more likely to desorb before it can become entrapped within a layer of ice (Ciesla et al. 2018). This effect is most obvious at 40 K and 50 K, in which CH_4 and CO entrapment remain high, while all entrapment is suppressed at temperatures much higher than the hypervolatile desorption temperature. This effect may on its own explain why there is such a strong dependence of entrapment efficiency on binding energy, though more detailed modeling is needed to establish this with certainty.

Our findings mirror the broad trends outlined by Bar-Nun et al. (1988) and Almayrac et al. (2022). Bar-Nun et al. (1988) tested multicomponent ice mixtures of CH_4, CO, N_2, and Ar at higher deposition temperatures. Unlike their experiments at low temperatures, Bar-Nun et al. (1988) find significant differences in relative entrapment efficiency across species at higher deposition temperatures, with the order of entrapment being $CH_4 > CO > N_2 \geqslant$ Ar. Almayrac et al. (2022) similarly find increasing differences in relative entrapment efficiency between N_2 and noble gases with increasing deposition temperature.

To test for the effects of competition between hypervolatiles, we conducted experiments with dilute and concentrated gas mixtures deposited at 50 K. If competition is significant, we would expect to see increasing differences in entrapment between different hypervolatiles with increasing concentration, since more hypervolatiles are competing for the same number of strongly binding sites. We do indeed find increasing differences in relative entrapment efficiencies when we increase hypervolatile-to-water concentration, suggesting that competition plays a role in setting the entrapment efficiency of the most volatile species in warmer ices, especially when the hypervolatiles are present at high concentration (Figure 9). Without detailed modeling or additional experiments, it is difficult to establish the relative importance of this effect as compared to hypervolatile residence time during deposition. However, based on the existing data, hypervolatile residence time appears to be the main driving factor for entrapment in dilute ice mixtures, which are most relevant in most astrophysical settings, while competitive entrapment becomes increasingly important with increasing hypervolatile concentration.

In summary, small differences in hypervolatile binding energies can result in large differences in entrapment efficiency if the ices are deposited close to the hypervolatile desorption temperature. These differences can be further enhanced by competitive entrapment in ices with relatively high hypervolatile concentrations.

4.3. Astrophysical Implications

Hypervolatile entrapment studies have at least three major applications: (1) explaining the presence of hypervolatiles in warm environments; (2) predicting hypervolatile abundances of planets and planetesimals, and hence their chemical trajectories; and (3) using measurements of hypervolatile abundance patterns to infer the formation conditions of a particular body. The latter could be especially powerful for comets, which are expected to be chemically pristine (Mumma & Charnley 2011). All of these applications are complicated by laboratory results revealing that entrapment efficiencies are sensitive to ice thickness, ice matrix composition, and hypervolatile concentration, in addition to ice formation temperature (Bar-Nun et al. 1988, 2007; Bar-Nun & Owen 1998; Collings et al. 2003; Fayolle et al. 2011; Almayrac et al. 2022). In our set of experiments, we have strived to investigate ice thicknesses and hypervolatile concentrations that are comparable to interstellar ices, which should also be appropriate for the initial icy grain population in protoplanetary disks prior to substantial grain growth. However, we do not take into account the full range of ice growth conditions and matrix compositions that exist in astrophysical environments. Thus, our findings can inform interpretations of hypervolatile abundances in interstellar and cometary ices, but any conclusions based on quantitative comparisons are at best provisional.

To illustrate how laboratory entrapment data can be used to better understand hypervolatile abundances in solar system objects, we calculate the expected hypervolatile abundances for ices formed at different temperatures. We note that these hypervolatile abundances are derived assuming that pure water entrapment is the sole hypervolatile retention mechanism, while in reality other mechanisms are known to affect hypervolatile abundances, including entrapment in CO_2, a significant component of cometary ice (Kouchi & Yamamoto 1995; Simon et al. 2019, 2023; Gudipati et al. 2023). Thus, the following calculations cannot be used to directly derive the formation temperature of observed cometary ices, but rather as a guideline for how hypervolatile entrapment affects the observed hypervolatile abundances in comets and related objects.

The final entrapped hypervolatile abundance of an icy grain, the building block of outer solar system bodies, is a product of the initial hypervolatile abundance and the hypervolatile entrapment efficiency. We therefore begin with estimating the initial hypervolatile abundances that are mixed with water under the assumption that the initial ice composition of the protosolar nebula is similar to that observed around other low-mass protostars. One complicating factor is that interstellar ices consist of water-rich and CO-rich ice phases, but for our purposes we only consider the H_2O-rich ice phase. Based on protostellar ice studies this water phase contains ∼13% of CO and 5% of CH_4 with respect to water (Öberg et al. 2011a; Boogert et al. 2015). We follow Öberg & Wordsworth (2019)

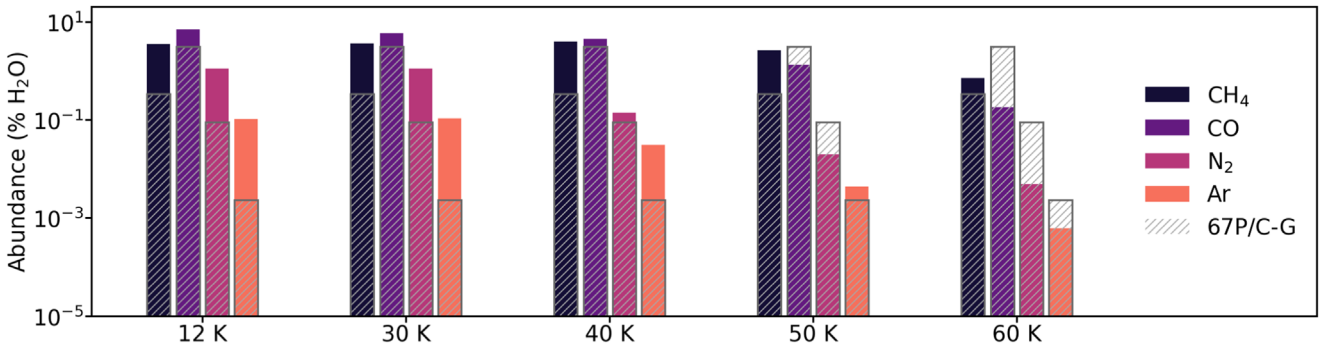

Figure 11. The predicted hypervolatile abundances derived from the estimated initial solar nebula composition (assuming that 13% of Ar is incorporated in water) and our experimental entrapment efficiencies at different deposition temperatures. The gray shaded bars, representing the observed volatile abundances in Comet 67P/C-G, are shown for illustration only, since entrapment efficiencies in comets are complicated by the presence of other matrix species, especially CO_2, and a history of multiple warm-up cycles. The volatile abundances are expressed in percentage of water abundance.

and estimate that the N_2 and Ar abundances with respect to water are 19% and 1.6%. Assuming that N_2 behaves similarly to CO, we estimate that only about 13% of the N_2 is incorporated into the water-rich ice phase, but note that future astrochemical models may predict a lower or higher N_2 abundance in the water ice phase. We assume that either 13% or 100% of the Ar budget is incorporated into the water ice. This gives us an approximate initial water ice composition of 100:5:13:2.4:0.2(1.6) for H_2O:CH_4:CO:N_2:Ar.

We then calculate the expected ice abundances due to entrapment if the ice is formed at different temperatures between 12 and 60 K by multiplying the experimentally derived entrapment efficiencies with the initial ice hypervolatile abundances. For illustration, we compare these with the hypervolatile abundances of the most well-studied comet to date (Figure 11 and Table 3): Comet 67P/Churyumov-Gerasimenko (hereafter 67P/C-G) from the Rosetta mission (Glassmeier et al. 2007). CH_4, CO, N_2, and Ar have all been observed in the coma of this comet (Balsiger et al. 2015; Rubin et al. 2020). Though none of the ice temperatures provide a perfect fit, which is not surprising considering the possible effects of more realistic ice matrices and ice evolutionary trajectories, most of the derived hypervolatile abundances are of the same order of magnitude as those found in the comet, indicating that entrapment provides a reasonable explanation for observed cometary hypervolatiles. More specifically, the CO and N_2 abundances of 67P/C-G fall in between the abundance predictions at 40 K and 50 K, the observed Ar abundance is closest to the prediction at 50 K, and the observed CH_4 abundance is substantially lower than the predicted abundance at any temperature. Even taking into account the uncertainties of the ice matrix, this latter result suggests that other mechanisms beyond a lack of entrapment are responsible for the low observed CH_4 abundance. Indeed, ice experiments have shown that CH_4 is rapidly converted into more complex organic molecules in the presence of UV or electrons, which may explain this discrepancy (Bergantini et al. 2017; Bergner et al. 2017; Carrascosa et al. 2020). In contrast, CO, N_2, and Ar range from chemically stable to inert, and so their abundances should more closely reflect their entrapment efficiencies. Here, however, we are prevented from any strong conclusions due to the possible impact of CO_2 as well as the precise ice formation and evolution dynamics on the final hypervolatile abundances. For example, in the Läuter et al. (2020) study of volatile gas production from 67P/C-G, it appears that the outgassing of CO and CH_4 correspond more closely with the desorption of CO_2 than that of water in the post-perihelion phase. Another uncertainty that arises when comparing laboratory results and cometary observations is that laboratory TPDs often heat the ice at a faster rate than would be expected in realistic scenarios. Further experimental investigation is needed in order to determine the degree to which heating rate impacts entrapment.

Table 3
Predicted Hypervolatile Abundances by Temperature, Given an Initial Protostellar Ice Composition

Temperature	CH_4	CO	N_2	Ar
Solar	5	13	2.4	0.2
12 K	3.50	6.89	1.10	0.104 (0.797)
30 K	3.65	5.72	1.10	0.106 (0.813)
40 K	3.95	4.42	0.136	0.030 (0.234)
50 K	2.60	1.30	0.020	0.004 (0.033)
60 K	0.70	0.182	0.005	0.0006 (0.005)
67P/C-G	0.34	3.1	0.09	0.0023

Notes. Values are in parts per 100 parts of water. The hypervolatile abundances for 67P/C-G are included for illustration only.

5. Conclusion

In this experimental study, we investigated the entrapment efficiencies of four astrophysically relevant hypervolatiles (CH_4, CO, N_2, and Ar) within H_2O ice matrices in three-component and five-component ice mixtures, concentrated and dilute ice mixtures, and at different deposition temperatures between 12 and 100 K. Our main findings are as follows.

1. For ices deposited at low temperatures and dilute concentrations, we observe small differences in entrapment efficiencies across species, which we theorize is primarily due to differences in each hypervolatile's binding energy to water, with no evidence for competitive entrapment.
2. We observe increasing differences in entrapment efficiencies across species with increasing deposition temperature. We theorize that this is mainly due to the strong dependence of entrapment on hypervolatile residence times during ice deposition close to the hypervolatile desorption temperature.

3. We observe increasing differences between entrapment efficiencies of different species with increasing hypervolatile concentration, especially when comparing CO to N_2 and Ar. This suggests that competition can play a role in concentrated ice mixtures, where the hypervolatile-to-water ratio approaches unity and strongly binding sites become scarce.
4. We use our experimental results to estimate hypervolatile abundances in ices formed at different temperatures and find reasonable agreement between ices formed at 40–50 K and observations of CH_4, CO, N_2, and Ar in Comet 67P/C-G. However, to conclusively use laboratory data to establish cometary formation conditions would require more complex ice matrices and a larger parameter study of the ice formation and warm-up conditions than were within the scope of this study.

Acknowledgments

The authors would like to thank Dr. Sean Andrews and Dr. Ramesh Narayan for providing thoughtful comments and feedback. The authors are also grateful to Dr. Elettra Piacentino for providing assistance with laboratory methods and interpretation. This project began as a junior thesis project at Harvard College, and feedback was also provided by other students in the course. K.I.Ö. acknowledges support from the Simons Foundation (SCOL #321183), and an award from the Simons Foundation (#321183FY19).

Appendix

The TPD curves for the repeated three-component and five-component experiments are represented in Figures A1 and A2, respectively.

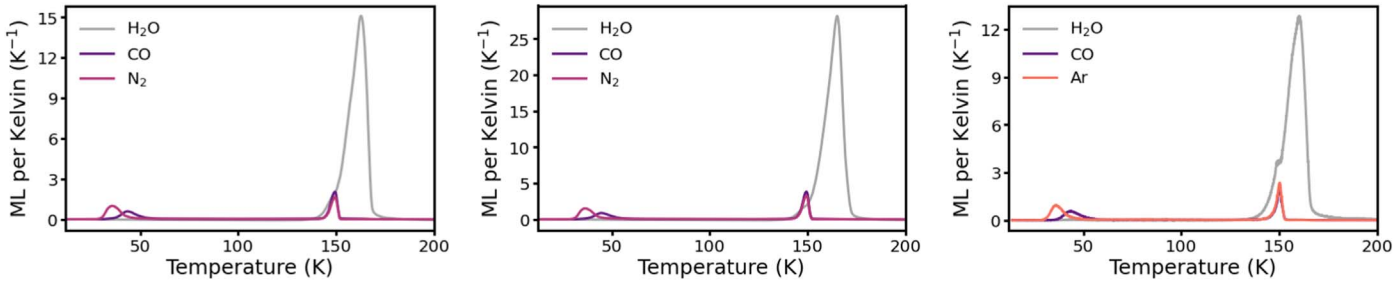

Figure A1. Continued from Figure 2: TPD curves for repeated three-component experiments deposited at 12 K and at a ratio of 10:1:1. The TPD curves for H_2O are included in these plots to illustrate the correlation between the desorption of water and the entrapped hypervolatiles. Water ice created at low temperatures is amorphous rather than crystalline, as would be expected in most astrophysical contexts (Stevenson et al. 1999; Kimmel et al. 2001). However, once the water ice reaches a sufficiently high temperature, it will crystallize, and the rearranging of the molecules will release many of the entrapped hypervolatiles close to the surface, referred to as volcano desorption (Collings et al. 2004; Simon et al. 2023). Thus, in the TPD curves, the peak desorption of the entrapped hypervolatiles occurs when the water ice crystallizes around 140 K. In many of the experiments, there is an additional small peak that coincides with water desorption (160 K), which corresponds to the remaining entrapped hypervolatiles co-desorbing with water.

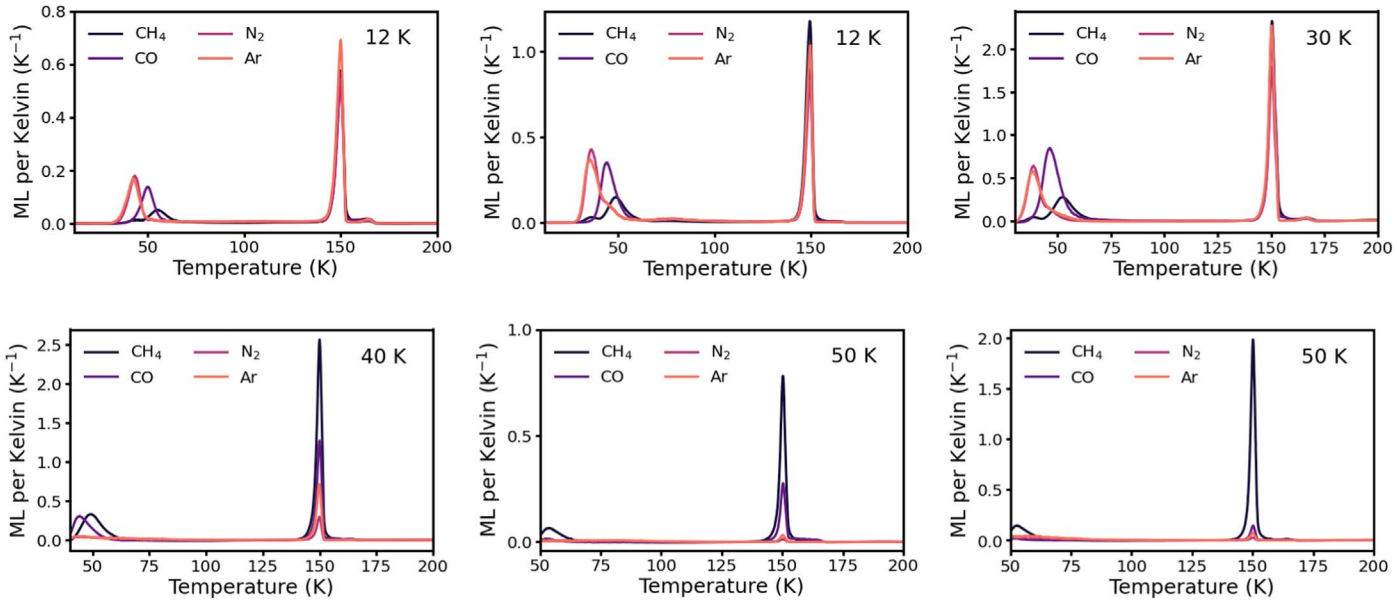

Figure A2. Continued from Figure 4: TPD curves for repeated five-component experiments deposited at varying temperatures and at a ratio of 20:1:1:1:1.

ORCID iDs

Qijia Zhou https://orcid.org/0000-0002-2028-8860
Alexia Simon https://orcid.org/0000-0002-5061-3054
Karin I. Öberg https://orcid.org/0000-0001-8798-1347
Mahesh Rajappan https://orcid.org/0000-0003-2761-4312

References

Almayrac, M. G., Bekaert, D. V., Broadley, M. W., et al. 2022, PSJ, 3, 252
Ayotte, P., Smith, R. S., Stevenson, K. P., et al. 2001, JGR, 106, 33387
Balsiger, H., Altwegg, K., Bar-Nun, A., et al. 2015, SciA, 1, e1500377
Bar-Nun, A., Herman, G., Laufer, D., & Rappaport, M. L. 1985, Icar, 63, 317
Bar-Nun, A., Kleinfeld, I., & Kochavi, E. 1988, PhRvB, 38, 7749
Bar-Nun, A., Notesco, G., & Owen, T. 2007, Icar, 190, 655
Bar-Nun, A., & Owen, T. 1998, in Astrophysics and Space Science Library, Vol. 227, Solar System Ices, ed. B. Schmitt, C. de Bergh, & M. Festou (Dordrecht: Kluwer), 353
Bergantini, A., Maksyutenko, P., & Kaiser, R. I. 2017, ApJ, 841, 96
Bergner, J. B., Öberg, K. I., & Rajappan, M. 2017, ApJ, 845, 29
Boogert, A. C. A., Gerakines, P. A., & Whittet, D. C. B. 2015, ARA&A, 53, 541
Bouilloud, M., Fray, N., Bénilan, Y., et al. 2015, MNRAS, 451, 2145
Carrascosa, H., Cruz-Díaz, G. A., Muñoz Caro, G. M., Dartois, E., & Chen, Y. J. 2020, MNRAS, 493, 821
Ciesla, F. J., Krijt, S., Yokochi, R., & Sandford, S. 2018, ApJ, 867, 146
Collings, M. P., Anderson, M. A., Chen, R., et al. 2004, MNRAS, 354, 1133
Collings, M. P., Dever, J. W., Fraser, H. J., & McCoustra, M. R. S. 2003, Ap&SS, 285, 633
Dodson-Robinson, S. E., Willacy, K., Bodenheimer, P., Turner, N. J., & Beichman, C. A. 2009, Icar, 200, 672
Fayolle, E. C., Öberg, K. I., Cuppen, H. M., Visser, R., & Linnartz, H. 2011, A&A, 529, A74
Fresneau, A., Danger, G., Rimola, A., et al. 2014, MNRAS, 443, 2991
Gerakines, P. A., & Hudson, R. L. 2015, ApJL, 805, L20
Gerakines, P. A., Materese, C. K., & Hudson, R. L. 2023, MNRAS, 522, 3145
Gerakines, P. A., Schutte, W. A., Greenberg, J. M., & van Dishoeck, E. F. 1995, A&A, 296, 810
Glassmeier, K.-H., Boehnhardt, H., Koschny, D., Kührt, E., & Richter, I. 2007, SSRv, 128, 1
Gudipati, M. S., Fleury, B., Wagner, R., et al. 2023, FaDi, 245, 467
Hudgins, D. M., Sandford, S. A., Allamandola, L. J., & Tielens, A. G. G. M. 1993, ApJS, 86, 713
Kimmel, G. A., Stevenson, K. P., Dohnálek, Z., Smith, R. S., & Kay, B. D. 2001, JChPh, 114, 5284
Kouchi, A., & Yamamoto, T. 1995, Prog. Cryst. Growth Charact. Mater., 30, 83
Läuter, M., Kramer, T., Rubin, M., & Altwegg, K. 2020, MNRAS, 498, 3995
Lectez, S., Simon, J. M., Mousis, O., et al. 2015, ApJL, 805, L1
Lewis, J. S. 1974, Sci, 186, 440
Lunine, J. I., & Gautier, D. 2004, in Comets II, ed. M. C. Festou & H. U. Keller (Tucson, AZ: Univ. Arizona Press), 105
Martín-Doménech, R., Manzano-Santamaría, J., Muñoz Caro, G. M., et al. 2015, A&A, 584, A14
Mousis, O., Guilbert-Lepoutre, A., Lunine, J. I., et al. 2012, ApJ, 757, 146
Mumma, M. J., & Charnley, S. B. 2011, ARA&A, 49, 471
Notesco, G., Bar-Nun, A., & Owen, T. 2003, Icar, 162, 183
Öberg, K. I., & Bergin, E. A. 2021, PhR, 893, 1
Öberg, K. I., Boogert, A. C. A., Pontoppidan, K. M., et al. 2011a, ApJ, 740, 109
Öberg, K. I., Murray-Clay, R., & Bergin, E. A. 2011b, ApJL, 743, L16
Öberg, K. I., & Wordsworth, R. 2019, AJ, 158, 194
Owen, T., Mahaffy, P., Niemann, H. B., et al. 1999, Natur, 402, 269
Pontoppidan, K. M., Dullemond, C. P., van Dishoeck, E. F., et al. 2005, ApJ, 622, 463
Rowland, B., Fisher, M., & Devlin, J. P. 1991, JChPh, 95, 1378
Rubin, M., Engrand, C., Snodgrass, C., et al. 2020, SSRv, 216, 102
Sasselov, D. D., & Lecar, M. 2000, ApJ, 528, 995
Simon, A., Öberg, K. I., Rajappan, M., & Maksiutenko, P. 2019, ApJ, 883, 21
Simon, A., Rajappan, M., & Öberg, K. I. 2023, ApJ, 955, 5
Stevenson, K. P., Kimmel, G. A., Dohnalek, Z., Smith, R. S., & Kay, B. D. 1999, Sci, 283, 1505
Villadsen, T., Ligterink, N. F. W., & Andersen, M. 2022, A&A, 666, A45